Supplementary Materials for

Atomic Mechanism of Metal Crystal Nucleus Formation in a Single-Walled Carbon Nanotube

Kecheng Cao[1], Johannes Biskupek[1], Craig T. Stoppiello[2], Robert L. McSweeney[2], Thomas W. Chamberlain[3], Zheng Liu[4, 5], Kazu Suenaga[4], Stephen T. Skowron,[2] Elena Besley,[2] Andrei N. Khlobystov[2,*], Ute Kaiser[1, *]

Affiliations:

[1]Central Facility for Electron Microscopy, Group of Electron Microscopy of Materials Science, Ulm University, 89081 Ulm, Germany

[2]School of Chemistry, University of Nottingham, University Park, Nottingham NG7 2RD, United Kingdom

[3]Institute of Process Research & Development, School of Chemistry, University of Leeds, Leeds, LS2 9JT, United Kingdom

[4]Nanomaterials Research Institute, National Institute of Advanced Industrial Science and Technology (AIST), Tsukuba, 305-8565 Japan

[5]Inorganic Functional Materials Research Institute, National Institute of Advanced Industrial Science and Technology (AIST), Nagoya, 463-8560 Japan

*Correspondence to: ute.kaiser@uni-ulm.de (U.K); andrei.khlobystov@nottingham.ac.uk (A.K.)

Table of contents:

Section 1. DFT calculations for studying the structures of Fe clusters

Density functional theory (DFT) calculations were performed at the BLYP/def2-TZVP level of theory [S1-3] using the Q-Chem 5.0 quantum chemistry software package [S4]. The SCF convergence criterion was 10^{-8} and the threshold for neglect of two electron integrals was 10^{-12} E_h. Single point energy calculations were performed for the Fe atom at odd spin multiplicities from 1 to 9, geometry optimisations of the Fe_2 dimer at odd multiplicities from 1 to 13, and geometry optimisations of the Fe_3 trimer at odd multiplicities from 1 to 19. All calculations employed Q-Chem's internal stability analysis procedure to ensure self-consistent field (SCF) convergence to true minima; SCF calculations frequently initially converged to saddle points, especially for systems involving the trimer and stretched dimers. Optimisations were followed by frequency

calculations to ensure that the geometries were minima (no imaginary frequencies were present).

A summary of the ground state energies and geometries of each species is given below:

Species	Ground state multiplicity	Bond length (nm)	Total electronic energy (E_h)	Atomisation energy (eV)
Fe atom	5	N/A	-1263.73053	N/A
Fe_2 dimer	7	0.203	-2527.54270	+2.22
Fe_3 trimer	11	C_{2v}: 0.233, 0.233, 0.220	-3791.35005	+4.31

Atomisation energies for Fe_N were calculated as (N * E(Fe)) – E(Fe_N).

To provide context for the discussion of the Fe diatomic seed observed in TEM (Figure 2, Supplementary Video 1), the energies of the dimer at several additional specific bond lengths were also calculated:

	Bond length (nm)	Ground state multiplicity	Total electronic energy (E_h)	Atomisation energy (eV)
DFT optimised dimer	0.20	7	-2527.54270	+2.22
Bulk γ-Fe	0.29	1	-2527.49714	+0.98
Fe_2@SWNT (0 - 13 s)	0.33	9	-2527.49093	+0.81
Fe_2@SWNT (13 s)	0.43	9	-2527.47005	+0.24

The precise nature of the electronic ground state of even the Fe dimer is poorly understood and remains controversial. Obtaining an accurate description of the electronic structure remains difficult, having been described as 'a Herculean labour' requiring multireference configuration interaction methods [S5]. However, the DFT method employed here – while obviously not providing a complete or accurate description of the electronic structure of the small iron clusters – is notable for accurately reproducing ground state geometries that agree very well with both experimental values and accurate multireference computational methods [S5-6], while remaining scalable beyond Fe_2.

The BLYP/def2-TZVP level of theory used predicts a septet ground state rather than the correct nonet, as previously reported for DFT methods [S6-7]. Interestingly, this nonet-septet inversion did not occur at the BLYP/6-31G* level of theory; however the use of the small Pople basis set resulted in very large basis set superposition errors in the calculated binding energies (> 1 eV for 6-31G* compared to < 0.02 eV for def2-TZVP).

Unfortunately, the use of DFT for accurately modelling geometries appears to be limited to very small iron clusters. The ground state of Fe_2 has an inherently multiconfigurational nature, with the dominating electronic configuration contributing only 73% of the ground state as calculated by RASPT2 [S6]. The unsuitability of attempting to model the increasingly multi-reference character of larger Fe_N clusters with a single reference method such as Kohn-Sham DFT manifests as severe issues with SCF convergence, limiting convergence to 10^{-5} E_h and below and having a subsequent impact on the accuracy of geometry optimisations. An additional complexity arises at cluster sizes of Fe_5 and above, for which the ground states have noncollinear magnetic

configurations [S8] in a similar fashion to the spin-spiral structure of γ-Fe [S9], requiring methods such as constrained DFT [S10].

The extreme difficulty of accurately modelling even several atoms of Fe, coupled with the limited experimental work on such species [S5], reinforces the importance of using atomic imaging techniques such as TEM to directly observe their structures, dynamics, and behaviour in real time and direct space.

Section 2. Electron-beam induced energy transfer

Compared to the nucleation investigated by liquid-cell TEM technology in which the complicated e-beam induced kinetic energy transfer (knock-on effect), heating, ionization and chemical reactions all occur simultaneously, the environment for the metal nucleation in our Metal@SWNT system is much simpler. The vacuum ambiance and constant temperature (room temperature) of the Metal@SWNT system makes the e-beam the sole energy source for the motion, nucleation and reaction of nanoclusters.

Elastic scattering and inelastic scattering between the incident electrons and atoms are the main interactions during TEM investigation. When the material has no bulk volume, the impact of secondary electrons and phonons is negligible. In addition, the SWNT possessing excellent thermal and electrical conductivity effectively mitigates heating and any ionization as stated in our previous published works [S11]. Thus, the kinetic energy transferred from incident electrons to the atoms by elastic scattering is the energy source for the motion, nucleation and reaction of nanoclusters in our experiments. The transferred kinetic energy increases the total free-energy of the nucleating cluster

which is similar to a heating process. The kinetic energy transferred from incident electrons to the nucleating cluster has a computable distribution as we have presented in Supplementary Figure 1. The maximum transferred kinetic energy depends on the energy of the incident electron and the atomic weight of the metal atoms. This electron beam irradiation process has many similarities to a normal heating process. Being heated, the nucleating cluster gains total free-energy by atom-atom collision and phonon absorption. The maximum gained free-energy is dependent on the temperature of the environment (the intensity of thermal motion of the system and the intensity of heat radiation). The energy transferred by an atom-atom collision has a distribution just like electron-atom interactions. Thus, we believe the nucleation processes of metal crystals activated by the electron beam irradiation are similar to those happening under thermal activation. Thus, the atomic details and discovered mechanism of nucleation processes we observed by electron beam should be transferrable to nucleation processes under other conditions.

The amount of kinetic energy transferred, E_T, from the e-beam to a stationary atom in this case is described as

$$E_T(\theta) = \frac{2m_nE(E+2m_ec^2)}{(m_n+m_e)^2c^2+2m_nE} sin^2\left(\frac{\theta}{2}\right) = E_{T\_max} sin^2\left(\frac{\theta}{2}\right) \qquad \text{(Supp. Eq. 1)}$$

where m_n is the mass of the atom, m_e is the mass of electron, θ is the electron scattering angle, and E is the energy of an electron.

The differential cross sections for elastic scattering were calculated using the relativistic Dirac partial-wave analysis [S12]. The scattering potential was obtained from the self-consistent Dirac-Hartree-Fock density for free atoms [S13] with the local exchange potential of Furness and McCarthy [S14]. The distributions of the differential

cross sections for the carbon, iron, rhenium and gold atom, which exist in the samples, are calculated using the NIST Electron Elastic-Scattering Cross-Section Database (Version 4.0) and shown in Supplementary Fig. 1 [S25].

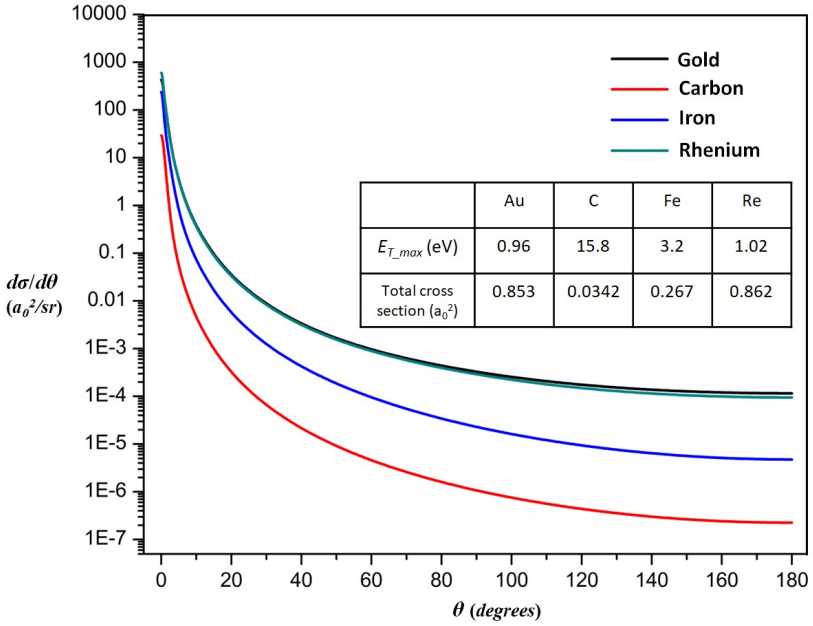

Supplementary Figure 1 | Differential cross sections of elastic scattering for Au, C, Fe and Re in $d\sigma/d\theta$ *versus* θ coordinates at 80 keV on logarithmic scales. The total elastic scattering cross sections of the metal atoms as well as the maximum transferred kinetic energy from the incident electrons to the atoms are listed in the inserted table. The Bohr radius, a_0, is the radius of the first Bohr orbit of the hydrogen atom where $a_0 = 5.2917721 \times 10^{-11}$ m and $a_0^2 = 2.8002852 \times 10^{-21}$ m^2.

Section 3. Atomic injector.

The SWNT based atomic injector plays an important role in this work transporting additional metal atoms to the diatomic seed or metal cluster. SWNT is a promising material to realize the transportation of molecules or atoms due to its narrow cylindrical cavities and mechanically robust structure. The molecules or nanostructures (including organic molecules, capsule-like amorphous carbon, LaC_2 nanoparticle and C_{60}) encapsulated in SWNT were observed to move under e-beam irradiation in TEM [S15-17]. The velocity of the moving particle is up to 112 nm/s as measured using a high speed camera. The driving mechanism of these motions has not been discovered and it remains conjecture that thermal gradients and momentum transfer between the electron beam and nanoparticles could be the driving force. Although the driving mechanism is not clear, the motions of nanoparticles under e-beam irradiation are successfully applied for *in situ* investigation of the nucleation of metal nanocrystals in this work. In Supplementary Fig. 2, the detailed time series in Fig. 1e in the main manuscript are presented.

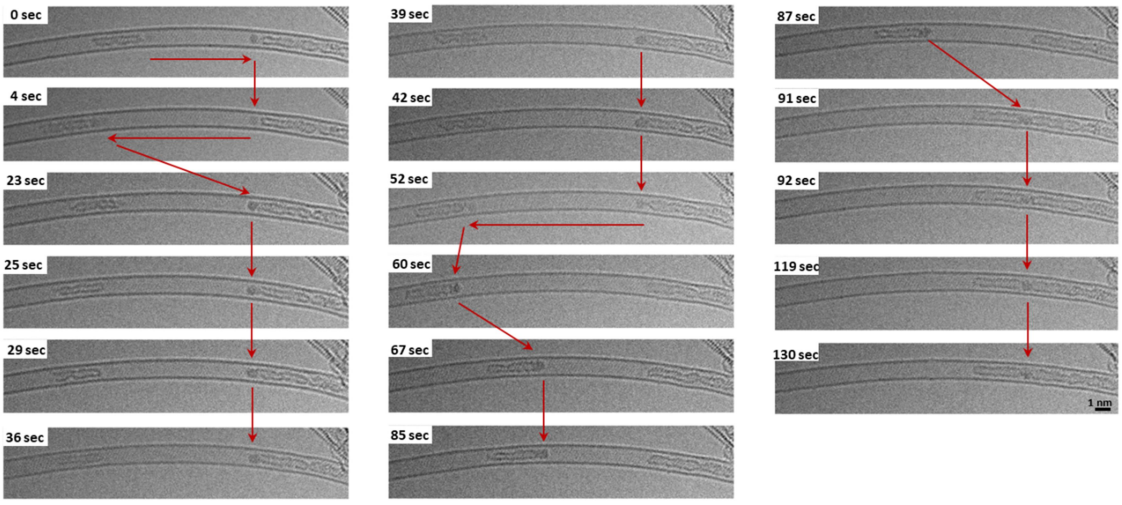

Supplementary Figure 2 | The detailed time-series AC-HRTEM images showing the motions of the Fe metal cluster and iron / amorphous carbon structure under 80 keV e-beam irradiation.

Section 4. Two-step nucleation mechanism with amorphous precursor

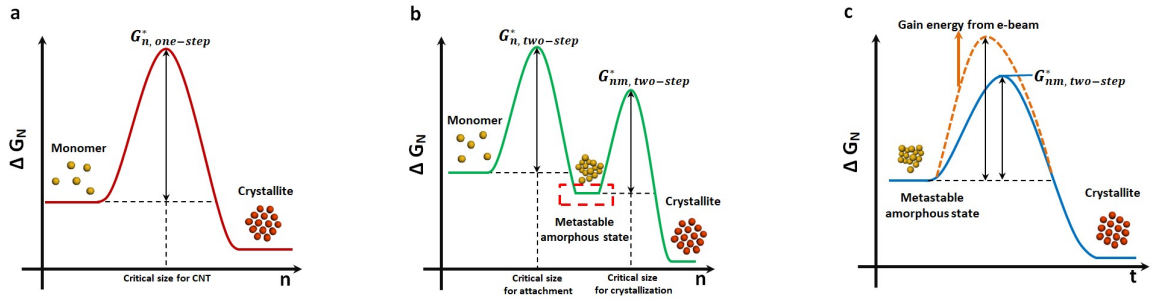

Supplementary Figure 3 | **a.** Sketch of the free energy difference for classical one-step nucleation theory, ΔG_N, as a function of the crystalline nucleus size n. A free energy barrier for nucleation, $G^*_{n,one-step}$, should be overcome to proceed from the dense agglomerate state to the thermodynamically stable crystalline phase. **b.** Sketch of the free energy difference ΔG_N as a function of the number of atoms in the cluster. In comparison to the classical one-step nucleation theory, TSNM involves a stable amorphous precursor stage from which an additional free energy barrier, $G^*_{nm,two-step}$, has to be overcome to reach the crystalline phase. **c.** Sketch of the free energy difference for the nucleation of an amorphous precursor larger in size than the critical size for crystallization in the TSNM framework using the energy from the incident e-beam to overcome the barrier to form the crystalline phase.

As described in the conventional thermodynamics of the crystal nucleation process, the free energy change required for cluster formation (ΔG_N) is written as the sum of the free energy change for the phase transformation (ΔG_V) and the free energy change for the formation of a surface (ΔG_S) [S18, S19]. In the classical one-step nucleation process (CNT), a free energy barrier for nucleation, $G^*_{n,one-step}$, must be overcome to proceed from the dense agglomerate state to the thermodynamically stable crystalline phase (Supplementary Fig. 3a). Whilst nowadays CNT nucleation theory is associated most often with crystallization from supersaturated solutions, it was initially derived for condensation of a vapor into a liquid, and has also been employed for crystallization from melts,− processes without solvent which are closer to the experimental conditions with which we study metals in nanotubes.

The CNT framework also requires a critical size of the nucleating cluster for direct nucleation to occur. For nucleation in solution, the ΔG_N of the cluster increases by gathering more atoms or ions, which helps overcome the free energy barrier. Thus, there is no stable amorphous state precursor in a classical one-step nucleation process. However, for the two-step nucleation process which incorporates an amorphous precursor, the gradually growing cluster must overcome the free-energy barrier for attachment and form a stable amorphous state precursor first; then grow further into a bigger metastable amorphous precursor and eventually overcome the free-energy barrier for crystallization, $G^*_{nm,two-step}$ (Supplementary Fig. 3b). The TSNM indicates that an amorphous precursor is necessary during the two-step nucleation process, and so its presence is an essential hallmark for the TSNM pathway and is directly observed and confirmed in our TEM experiments. In this research, we also observed a pre-existing Au

amorphous precursor which has a fixed number of atoms and overcomes the $G^*_{nm,two-step}$ by gaining energy from the incident e-beam (Supplementary Fig. 3c).

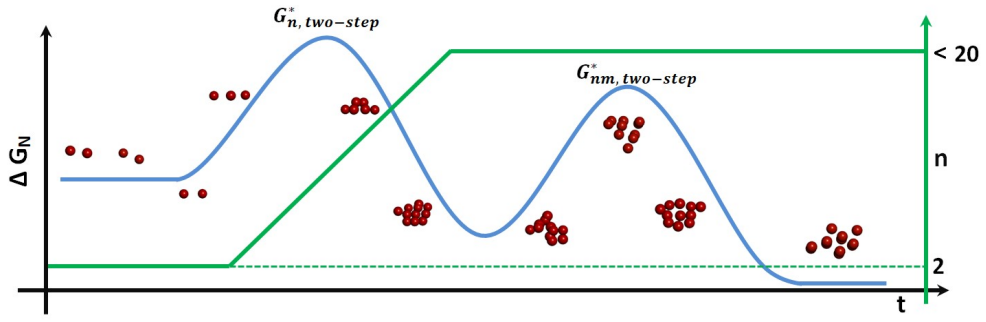

Supplementary Figure 4 | Proposed changes in the free energy ΔG_N and number of Fe atoms n along the nucleation time of γ-Fe's nucleation shown in Fig. 2 and Fig. 3. The energy diagram proposed on the basis of the observed size and shape of the Fe cluster in our experiment illustrates the changes of ΔG_N during the heterogeneous nucleation process of the γ-Fe nanocrystal. The Fe dimer is stabilized by the host SWNT which still could be dissociated by the 80 keV electron beam as shown in Supplementary Figure 7. Thus, the critical size for Fe atom attachment should be larger than two atoms.

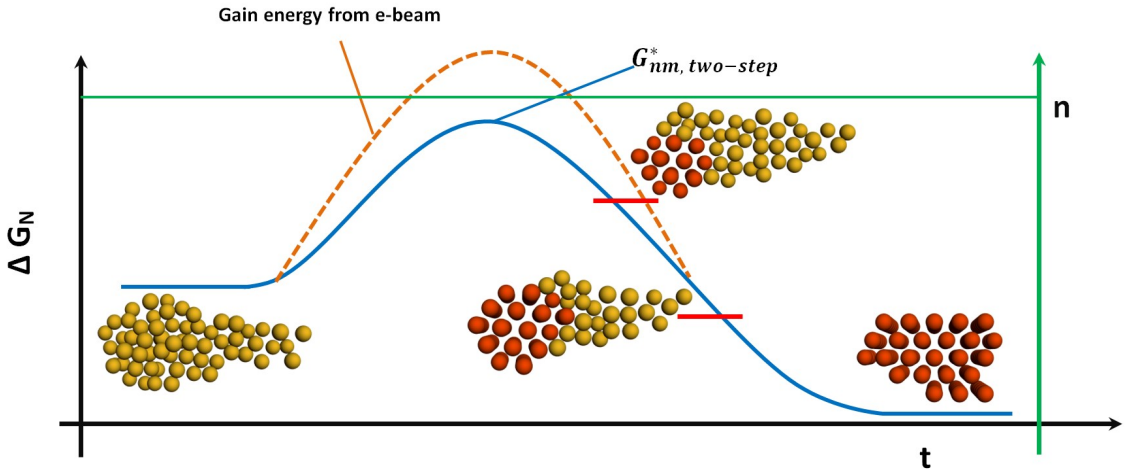

Supplementary Figure 5 | Proposed changes in the free energy ΔG_N and number of Au atoms n along the nucleation time during Au nucleation shown in Fig. 4. Although the shape of the Au cluster changes during the e-beam stimulated nucleation process, the number of the Au atoms keeps constant.

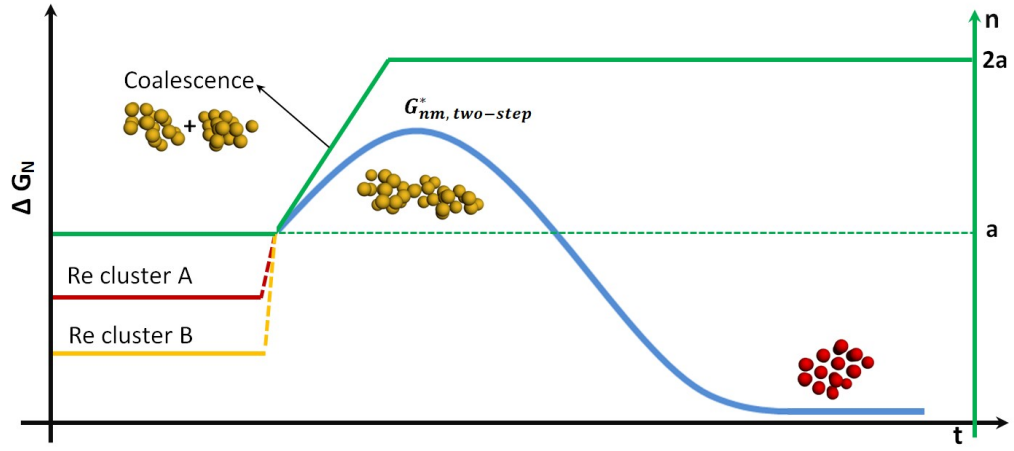

Supplementary Figure 6 | Proposed changes in the free energy ΔG_N and number of Re atoms n along the nucleation time of Re nanoclusters nucleation shown in Fig. 5. The coalescence of the two small pre-existing amorphous Re clusters A and B immediately increased the total free energy ΔG_N of the resultant Re cluster which helps the coalesced Re cluster overcome the energy barrier for crystallization and then transition into a Re crystallite. The number of atom, **a**, is about 10.

Section 5. Nucleation of γ-Fe crystallite

Here we present more experimental results to support the observation of heterogeneous nucleation of γ-Fe shown in Figure 2 and 3. In Supplementary Figure 7, we present the experimental evidence showing the Fe dimer on the wall of SWNT is not

stable under 80 keV electron beam irradiation. The bonding between the Fe dimer and the SWNT wall is partly destroyed by the electron beam, followed by dissociation of the Fe dimer by an incident electron. The Fe dimers on the wall of SWNT are relatively stable at room temperature without electron beam irradiation. The interaction between the dimer and the carbon atoms stabilizes the structure of the dimer. However, these dimers are not stable under our experimental conditions (at room temperature and under 80 keV electron beam irradiation) and are able to dissociate into single atoms. Thus, we have illustrated that - under our experimental conditions - the free-energy barrier of attachment for metal nucleation exists and the critical size for forming an amorphous cluster is larger than two atoms. In addition, the host SWNT acts as a substrate for stabilizing the seed for nucleation by physical and/or chemical interactions. This is a common phenomenon for nucleation in nature, in which nucleation processes happen at the gas- solid, gas- liquid and solid-liquid interface.

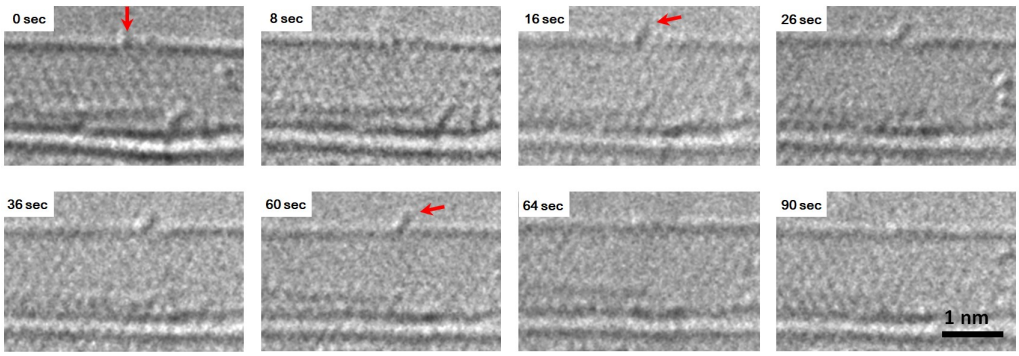

Supplementary Figure 7 | Time-series images showing a Fe dimer on the wall of a SWNT dissociating under an 80 keV electron beam. As indicated by red arrows, the interaction between the Fe dimer and the SWNT wall is partly destroyed by energy from

incident electrons, with the dimer protruding from the sidewall after 16 seconds' irradiation. The protruding Fe dimer then dissociated in the following 48 seconds.

In the heterogeneous nucleation of γ-Fe shown in Figure 2 and 3, the Fe dimer grew by ~ 15 Fe atoms in 16 seconds and became a Fe cluster larger than the critical size for nucleation. Thus, there is a possibility that the crystallization is just caused by relaxation from a high energy state, and it is necessary to prove the existence of a stable and intrinsically amorphous Fe cluster below this critical size. Here, Supplementary Figure 8 shows an intrinsically amorphous Fe cluster with approximately less than 10 Fe atoms ceaselessly changing its shape under 80 keV electron beam irradiation. During more than 240 seconds' observation, this Fe cluster keeps its disordered phase and does not dissociate into smaller clusters or single Fe atoms nor nucleate into a crystallite. Supplementary Figure 9 shows another intrinsically amorphous Fe cluster in a carbon 'atomic injector' that exhibits similar behaviour, keeping its disordered phase for more than 93 seconds' 80 keV electron beam irradiation. These two new time-series images directly prove that Fe clusters with a few Fe atoms (less than 17) confined in SWNTs are intrinsically amorphous at room temperature without electron beam irradiation and keep their disordered phase during TEM imaging by the 80 keV electron beam. Furthermore, the two small Re clusters before coalescence in Figure 5 of the main text are also intrinsically amorphous before TEM investigation and keep their disordered phases during the first 140 seconds of the TEM imaging. Thus, the disordered phase of precursors for the metal nucleation with very small size is stable.

As we explained in Section 1. Materials and Methods, we unfortunately did not record more images after the γ-Fe formed although we observed that it kept its crystalline

structure under the e-beam. In Supplementary Figure 10 we present an additional experiment showing that a γ-Fe crystallite with a diameter of approximately 1 nm and 100 Fe atoms keeps its crystalline structure under 80 keV electron beam irradiation to support our statement.

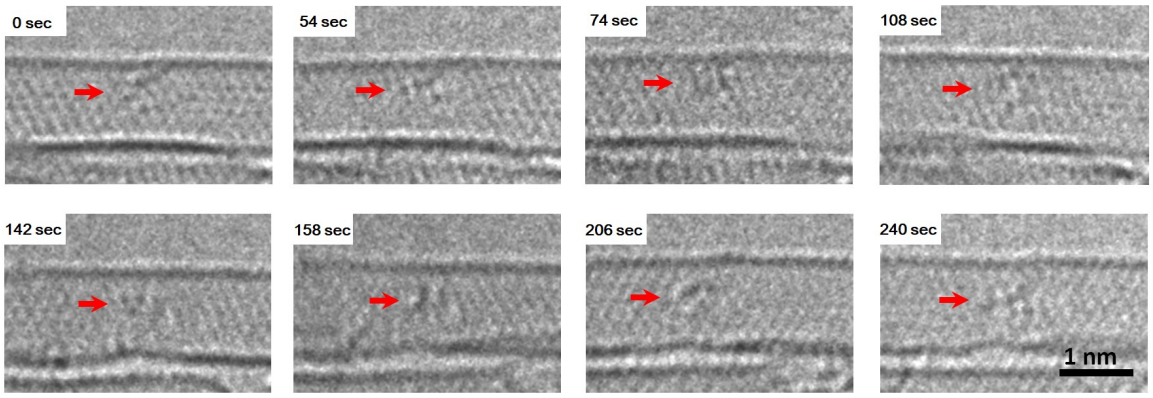

Supplementary Figure 8 | Time-series images showing that a small disordered Fe cluster with fewer than 10 atoms keeps changing its structure for over 240 seconds under 80 keV electron beam irradiation as indicated by red arrows. This amorphous Fe cluster is stable and does not dissociate into smaller clusters or single Fe atoms.

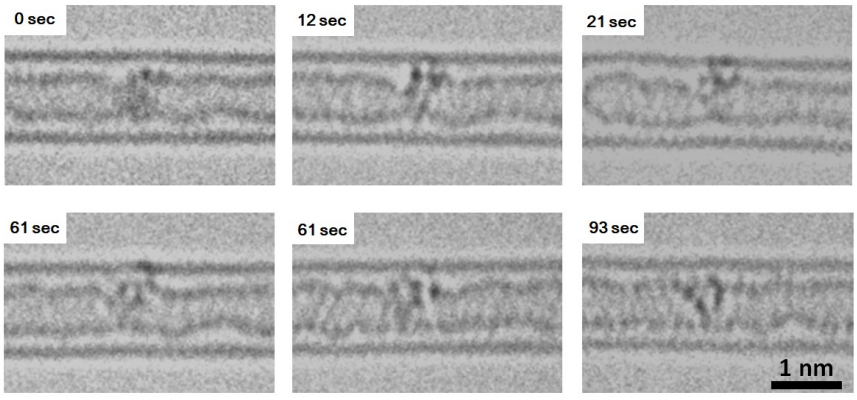

Supplementary Figure 9 | Time-series images showing a small disordered Fe cluster with fewer than 10 atoms in a carbon 'atomic injector' keeps changing its structure for

over 93 seconds under 80 keV electron beam irradiation. This amorphous Fe cluster interacts with the carbon 'atomic injector' and also the SWNT which could reduce its total free energy. This Fe cluster is also stable and does not dissociate into smaller cluster or single Fe atoms.

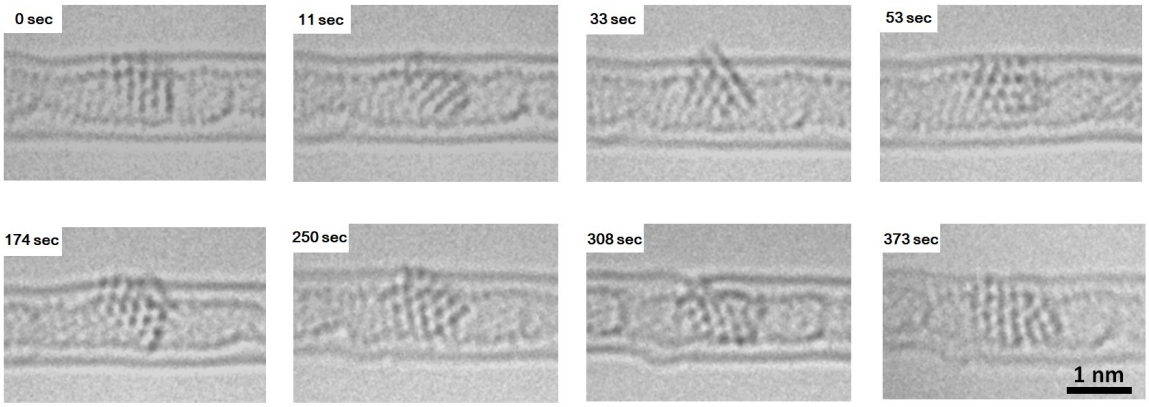

Supplementary Figure 10 | Time-series images showing that a γ-Fe crystallite in a carbon 'atomic injector' keeps its crystalline structure under 80 keV electron beam irradiation. This γ-Fe crystallite has a diameter of approximately 1 nm and contains approximately 100 Fe atoms.

Section 6. Crystallinity of the cluster

It is important to understand the real atomic structure of the cluster during the nucleation process. Here we present our approach for quantifying the crystallinity of the clusters and crystallite in our experiments. Compared to the metal nucleation in solution investigated by liquid-cell TEM, for example, the nucleation of Au in solution [S19,S20], the nucleated Au crystallite nucleus with a diameter of 0.90 nm in our experiment is much smaller. The size of the nucleated nucleus could be influenced by the different experimental conditions. Furthermore, due to factors including the silicon nitride

windows and the presence of water molecules in the liquid-cell TEM, the crystalline structure of a small crystallite (< 2 nm) formed in solution is unresolvable.

The metal clusters in our experiments are all dynamic under e-beam irradiation. Only when the cluster is imaged parallel to a low-indexed zone axis can its crystalline structure be resolved. As shown in Supplementary Fig. 11, we simulated TEM images (with a dose of 4.8×10^{7} e^{-} nm^{-2}) of two near-spherical Au crystallites with radii of 5 Å and 10 Å, one near-spherical amorphous Au cluster (radius of 10 Å) containing a crystalline core (radius of 5 Å) and one near-spherical amorphous Au cluster with a radius of 5 Å. The corresponding FFTs of these simulated TEM images are also presented for analyzing the reflection spots from the probable characteristic diffraction spot areas where the Au-reflections appear.

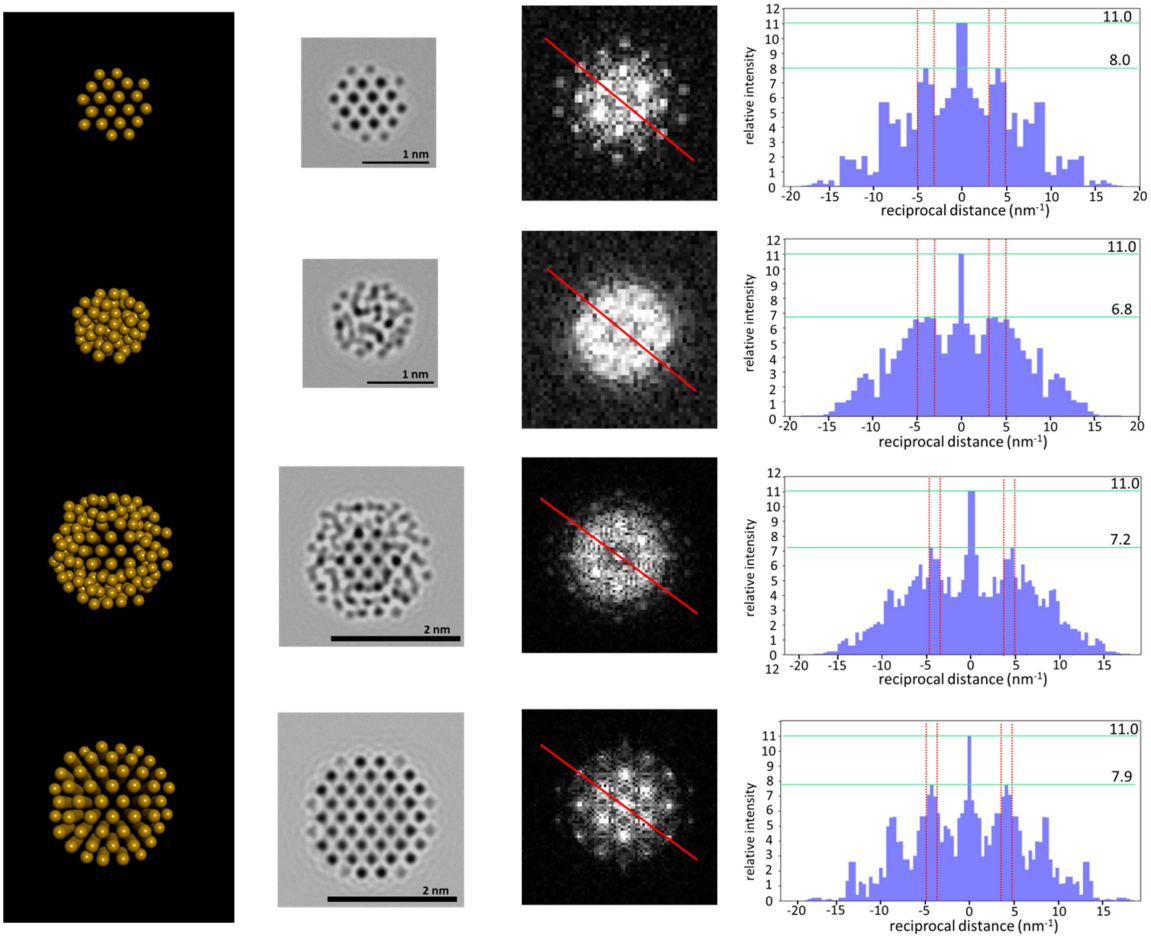

Supplementary Figure 11 | Approach for quantifying the crystallinity of clusters. **(The first column)** Models of near-spherical FCC Au crystallite with a radius of 5 Å, near-spherical Au amorphous cluster with a radius of 5 Å, near-spherical amorphous Au cluster (radius of 10 Å) containing a crystalline core (radius of 5 Å) and near-spherical fcc Au crystallite with a radius of 10 Å successively. **(The second column)** Simulated TEM images (80 kV, dose of 4.8×10^{7} $e^{-}nm^{-2}$) corresponding to the clusters in the same row. **(The third column)** FFT from the corresponding simulated TEM images in the same row. **(The fourth column)** Profiles corresponding to the red profile lines in the FFT of the same row. The first order 'reflection spots' in the FFT for the (111) fcc Au

crystallite face are around -4.26 nm^{-1}, the corresponding 'reflection spots area' (3.7 nm^{-1} to 4.9 nm^{-1} and -3.7 nm^{-1} to -4.9 nm^{-1}) are indicated by red dotted lines.

The modulus intensity of the first order 'reflection spots' for the two near-spherical Au crystallites with radii of 5 Å and 10 Å are 8.0 and 7.9. The corresponding value of the amorphous Au clusters containing a crystalline core is 7.2. The relative intensity of the strongest 'reflection spots' in the 'reflection spots area' of the FFT of amorphous Au cluster (radius of 5 Å) is 6.8. The two (111) Au crystallites are fully crystallized and show similar high relative intensity of the 'reflection spots'. The relative intensity of the 'reflection spots' for the partially crystallized cluster is lower. The relative intensity of the 'reflection spots' for the amorphous cluster is the smallest. Thus, there is a direct correlation between the relative intensity of the 'reflection spots' and crystallinity. ***By analyzing the modulus intensity of the strongest 'reflection spot' in the 'reflection spots area', the crystallinity of clusters during the nucleation processes is quantized and compared to each other.***

The crystallinities of the Fe, Au and Re clusters in Fig. 3, 4 and 5 are analyzed using the same method, normalising the intensity at different electron doses by comparing the intensity of the center pixel in the FFT. The 'reflection spots area' for Fe is from 4.0 nm^{-1} to 4.3 nm^{-1} and -4.0 nm^{-1} to -4.3 nm^{-1} ((111) face); and for Re is from 3.8 nm^{-1} to 4.3 nm^{-1} and -3.8 nm^{-1} to -4.2 nm^{-1} ((111) face).

In addition, the shape and the orientation of cluster could also influence our judgment of the structure of the particle from a 2D TEM image. To interpret this question, control TEM image simulations with corresponding FFT analysis have been carried out and presented in Supplementary Figure 12 and Supplementary Figure 13. In

Supplementary Figure 12, we compare the simulated TEM images and corresponding FFT patterns of a regular small Au crystallite and a less regular Au crystallite (that is, one with the same short range order but a lower degree of long range order) with the same atom number (32 Au atoms) from different titled angles. Supplementary Figure 12a is a regular Au crystal with (100) face which has a relative intensity of 8.2 for the strongest reflective spots except the central spot in FFT pattern. When it is tilted to another aligned face (Supplementary Figure 12a and b), the strongest reflective spots still show strong intensity. But when it is tilted to an angle deviating from a specific crystalline face as shown in Supplementary Figure 12d as an example, the periodic information shown in the 2D simulated TEM image is obviously reduced and the intensity of the strongest reflective spots decreases to 6.8. The Au crystallite in Supplementary Figure 12e is less regular with fewer periodic features. Therefore, the intensities of the strongest reflective spots for FFT patterns of the simulated TEM image of the less regular Au crystallite with different aligned faces are slightly reduced but still distinguishable (Supplementary Figure 12e,f,g). When this less regular Au crystallite is tilted to an angle deviating from a specific crystalline face (Supplementary Figure 12h), the intensities of the strongest reflective spots are significantly reduced which make it impossible to identify its crystalline structure. Actually, for even a small regular crystallite, its crystalline structure cannot be distinguished when it is tilted or rotated to an angle deviating from a specific crystalline face. In Supplementary Figure 13, we present a more detailed analysis for studying the influence of tilting. It shows the simulated TEM image and corresponding FFT analysis of the small regular Au crystal in Supplementary Figure 12a with 36 sets of titled angles along x and y directions. In these 36 sets, the strongest reflective spots of 28

sets have intensity over 7.2 which can be distinguished from amorphous structure according to our discussion presented above. That means, strictly speaking, it is not scientific to identify the amorphous structure of a small cluster only by analysing the periodic features of one TEM image.

Although it is unreasonable to identify the amorphous structure of a small cluster from a single TEM image, we are still able to evaluate the atomic structure (amorphous or crystalline) of the nucleating cluster by continuously observing and acquiring time-series TEM images. If a small cluster is amorphous, it is not possible to get a single TEM image showing obvious periodic feature from this amorphous cluster no matter how long the observation lasts. If a small cluster is crystalline, we always have the chance to get TEM images showing obvious periodic feature of the small crystallite during continuous observation, although in some frames the crystal looks amorphous owing to the angle at which the crystallite is tilted. Thus, we believe that continuous in-situ observation and atomic resolution are necessary for studying the nucleation of metal which cannot be achieved by either cryo-TEM (no continuous observation nor atomic resolution for sub-2nm cluster) or liquid-cell TEM (no atomic resolution for sub-2nm cluster).

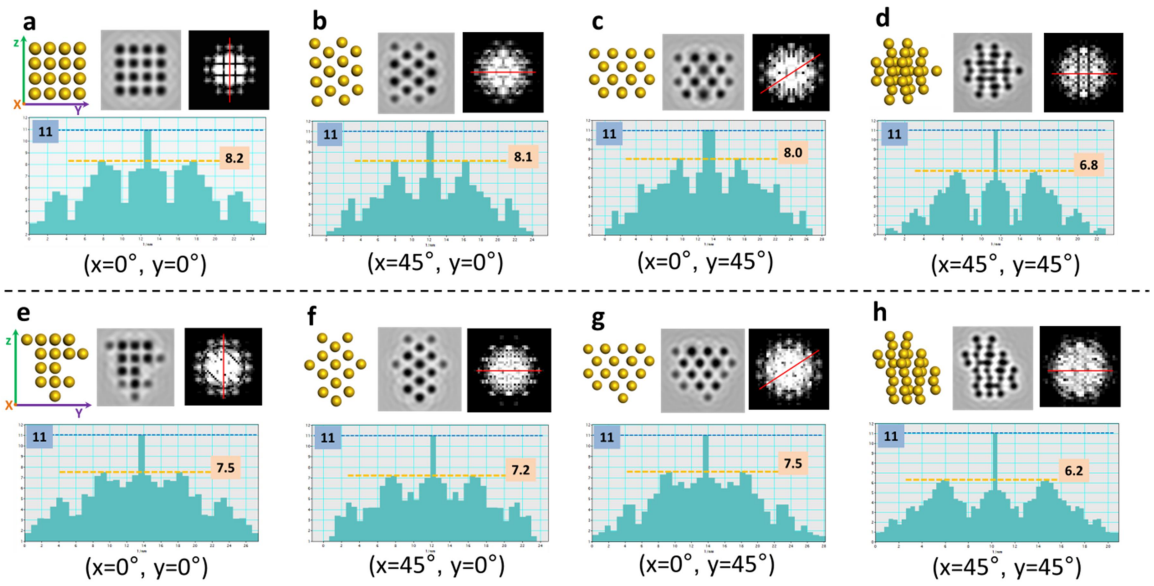

Supplementary Figure 12 | **a.** Structural model, corresponding simulated TEM image, FFT pattern and intensity profile of the red line in the FFT pattern of a regular FCC Au crystallite containing 32 atoms and showing the (100) face. The relative intensity of the strongest reflective spots except the central spot is 8.2 as indicated. **b-d.** Analysis sets as in (a) of the tilted Au crystallite in (a) with different angles as indicated. The tilting is along the x and y axis as shown in (a). **e.** Analysis sets as (a) of a less regular Au crystallite containing 32 atoms and showing the (100) face. The relative intensity of the strongest reflective spots except the central spot is 7.5 as marked. **f-h.** Analysis sets as (a) of the titled Au crystallite in (e) with different angles as indicated. The scale of the simulated TEM images is 1.20*1.20 nm.

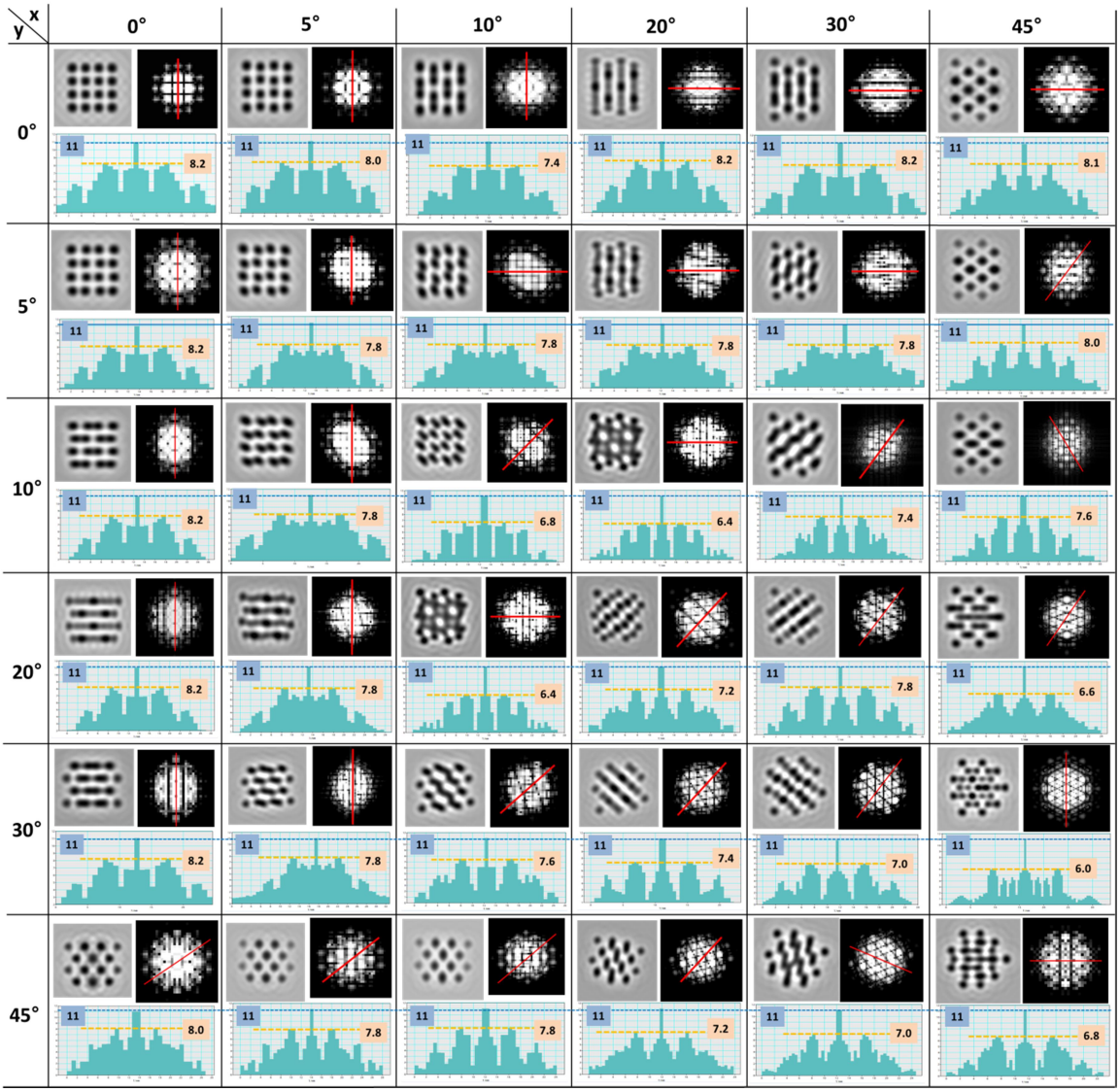

Supplementary Figure 13 | Simulated TEM images, corresponding FFT patterns and intensity profiles of the red lines in the FFT patterns of the regular FCC Au crystallite in Supplementary Figure 12 titled to different angle pairs along the axis indicated in Supplementary Figure 12a. The relative intensity of the strongest reflective spots except the central spot are all indicated.

Section 7. Determination of the number of atoms in the γ-Fe crystallite

The number of atoms in the cluster during the nucleation greatly determines the surface free energy and volume free energy of the cluster and further the whole progress of nucleation. Thus, it is critical to investigate the number of atoms in the clusters in our experiments. However, the Au cluster and Re clusters in Fig. 4 and Fig. 5 each contain over 20 atoms, making it almost impossible to figure out the number of atoms precisely. However, the Fe cluster in Fig. 3 contains significantly fewer Fe atoms making analysis of the number of atoms by TEM image simulation and contrast comparison possible. In supplementary Fig. 8, the chiral indices of the SWNT in the γ-Fe nucleation process is determined to be (n = 18, m = 2) [S21].

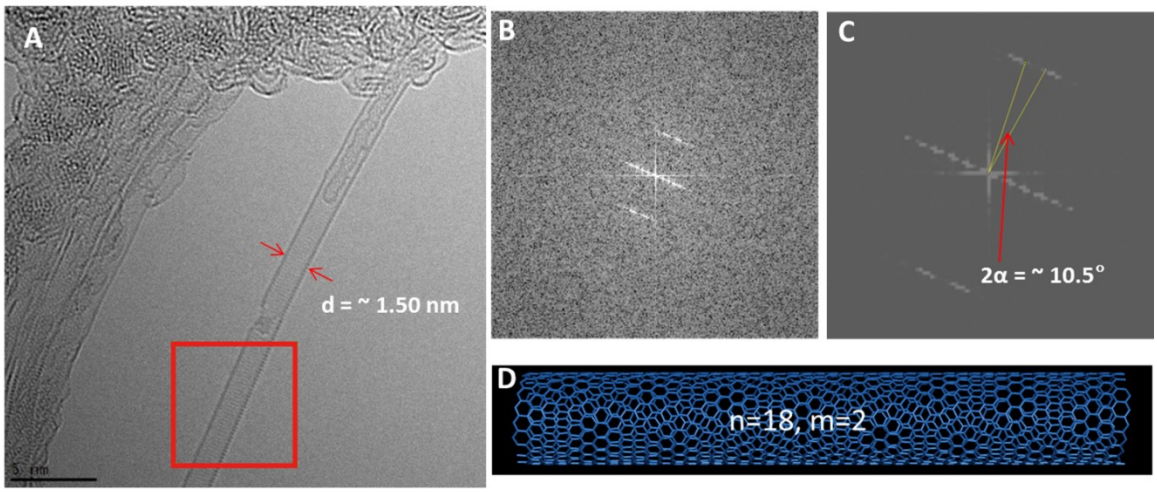

Supplementary Figure 14 | Measuring the chiral indices of SWNT. a. TEM image at 343 s from Supplementary Video 1. The diameter of this SWNT is about 1.50 nm. **b**. Fast Fourier transform pattern from the frame in **a**. **c.** High-contrast pattern of **b**, the doubled helical angle of the SWNT is about 10.5°. **d.** Simulated SWNT with chiral indices of (n = 18, m = 2).

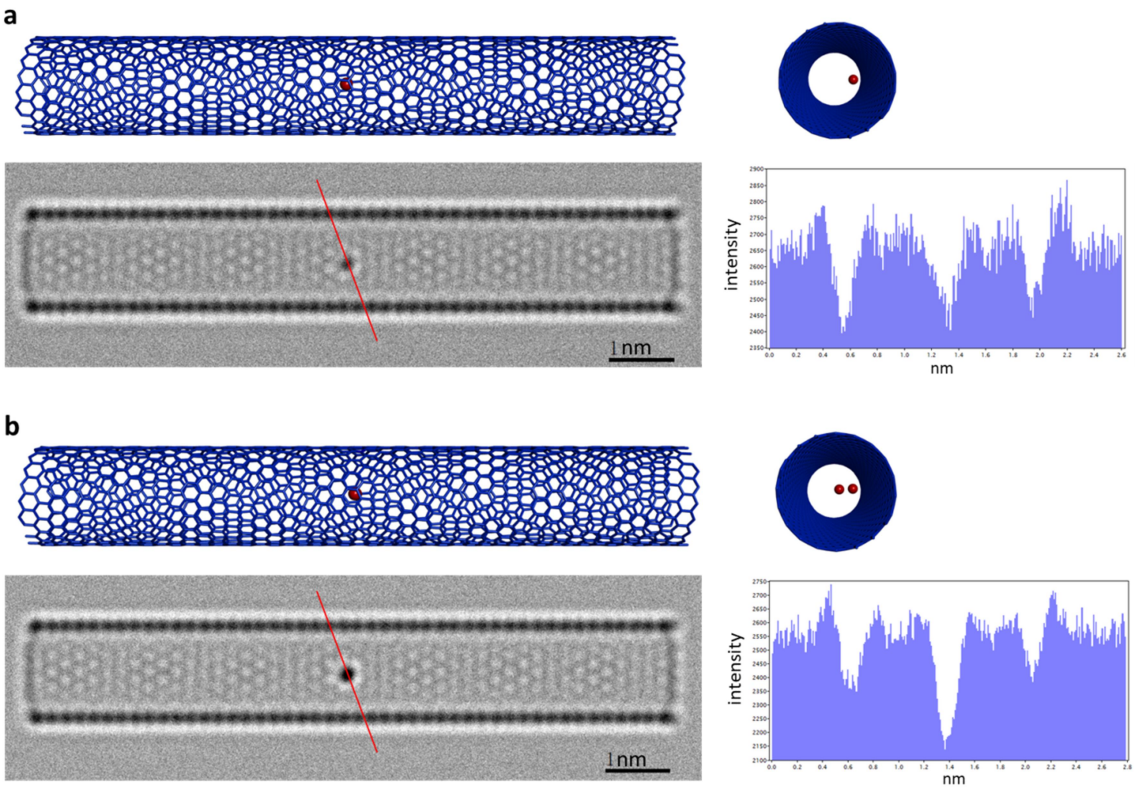

Supplementary Figure 15 | TEM image simulation showing the number of metal atoms along the e-beam direction distinguished by comparing contrast. The TEM images of the modeled structures of SWNT containing one (a) and two (b) Fe atoms are simulated with the same conditions used in the real TEM experiments shown in Fig. 2 and Fig. 3. The difference between the intensities of these two Fe spots demonstrates that the number of atoms along the e-beam direction is distinguishable.

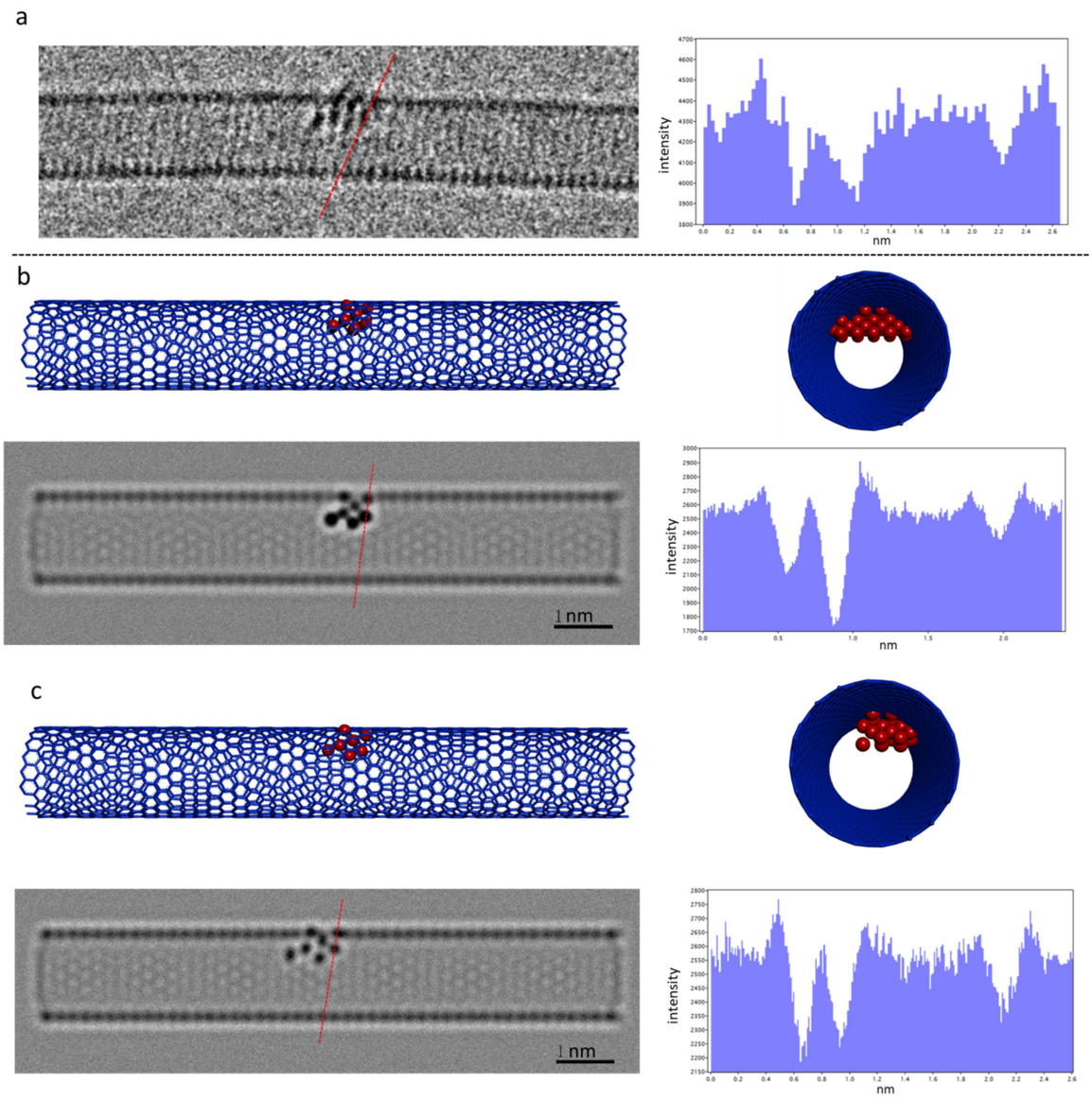

Supplementary Figure 16 | Simulated γ-Fe crystallite in a SWNT to determine the number of Fe atoms in the γ-Fe crystallite. a. The intensity profile of the γ-Fe crystallites in the raw TEM image. **b.** The possible maximal γ-Fe crystallite containing 27 Fe atoms which can fit into the host nanotube. The corresponding simulated TEM image shows the real γ-Fe crystallite should have fewer Fe atoms. **c.** A γ-Fe crystallite containing 17 Fe atoms shows similar intensities of Fe spots compared to the raw TEM

image demonstrating that it could be the real structure of the γ-Fe nucleus in Figure 4a at 197 s.

Section 8. SWNT cutting process by the γ-Fe crystallite

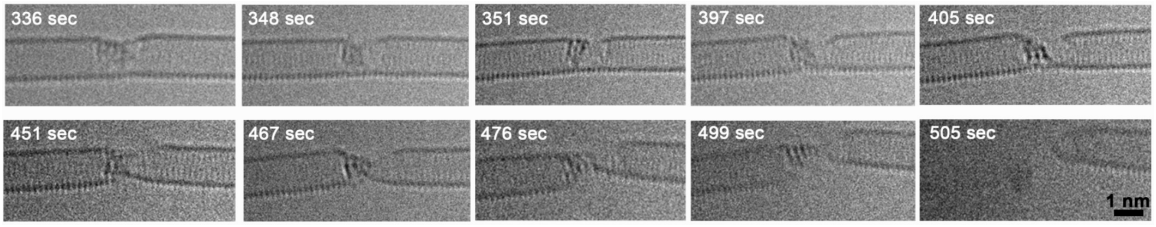

Supplementary Figure 17 | AC-HRTEM images presenting the electron beam driven nanotube cutting process catalyzed by the γ-Fe crystallite.

Since neither the diatomic Fe seed nor the amorphous Fe cluster exhibits such dramatic activity towards the nanotube, the increased reactivity of the γ-Fe nucleus may be related to changes in the Gibbs free energy of the metal cluster during the reorganization process. In order to understand why the γ-Fe crystallite interacts so strongly in the latter stage of the formation process, it is instructive to consider our recent studies on the catalysis of defect formation in SWNT by nickel and osmium clusters [S22, S10]. While the chemical properties of Fe, Ni and Os are very different, comparison of the AC-HRTEM observations for Fe with these previous studies reveals striking similarities between the three unrelated metals: in all three cases the metal cluster becomes more reactive towards the nanotube once the atoms in the cluster adopt a more ordered arrangement, e.g. becomes more crystal-like. Detailed molecular dynamics calculations, utilized previously to explore the atomistic mechanisms for a Ni cluster bonding and interactions with a SWNT under similar conditions, reveal that the surface of the metal cluster acts as a heterogeneous catalyst promoting the dissociation of the C-C bonds in the nanotube

sidewall [S22, S10]. Clearly, having regular inter-atomic spacing, implying a well-defined, ordered cluster surface, such as the ordered crystallographic plane required in an effective metal heterogeneous catalyst, is critically important for the effective activation of the covalent bonds in reactant molecules, including the C-C bonds in a SWNT, which explains the enhanced reactivity of the ordered metal clusters towards the nanotube [S23, S24].

References

S1. Becke, A. D. Density-functional exchange-energy approximation with correct asymptotic behavior. *Phys. Rev. A* **38**, 3098–3100 (1988).

S2. Lee, C., Yang, W. & Parr, R. G. Development of the Colle-Salvetti correlation-energy formula into a functional of the electron density. *Phys. Rev. B* **37**, 785–789 (1988).

S3. Weigend, F. & Ahlrichs, R. Balanced basis sets of split valence, triple zeta valence and quadruple zeta valence quality for H to Rn: Design and assessment of accuracy. *Phys. Chem. Chem. Phys.* **7**, 3297 (2005).

S4. Shao, Y. et al. Advances in molecular quantum chemistry contained in the Q-Chem 4 program package. *Mol. Phys.* **113**, 184–215 (2015).

S5. Kalemos, A. Fe_2: As simple as a Herculean labour. Neutral (Fe_2), cationic (Fe_2^+), and anionic (Fe_2^-) species. *J. Chem. Phys.* **142**, 244304 (2015).

S6. Hoyer, C. E., Manni, G. L., Truhlar, D. G. & Gagliardi, L. Controversial electronic structures and energies of Fe2, Fe2+, and Fe2− resolved by RASPT2 calculations. *J. Chem. Phys.* **141**, 204309 (2014).

S7. Gutsev, G. L. & Bauschlicher, C. W. Electron Affinities, Ionization Energies, and Fragmentation Energies of Fe n Clusters (n = 2−6): A Density Functional Theory Study. *J. Phys. Chem. A* **107**, 7013–7023 (2003).

S8. Alonso, J. A. Electronic and Atomic Structure, and Magnetism of Transition-Metal Clusters. *Chem. Rev.* **100**, 637–678 (2000).

S9. Oda, T., Pasquarello, A. & Car, R. Fully Unconstrained Approach to Noncollinear Magnetism: Application to Small Fe Clusters. *Phys. Rev. Lett.* **80**, 3622–3625 (1998).

S10. Cuadrado, R., Pruneda, M., García, A. & Ordejón, P. Implementation of non-collinear spin-constrained DFT calculations in SIESTA with a fully relativistic Hamiltonian. *J. Phys. Mater.* **1**, 015010 (2018).

S11. Cao K. et al. Comparison of atomic scale dynamics for the middle and late transition metal nanocatalysts. *Nat. Commun.* **9**, 3382 (2018).

S12. Walker D. W. Relativistic effects in low energy electron scattering from atoms *Advances in Physics,* **20,** 257-323 (1971)

S13. Desclaux J. P. A multiconfiguration relativistic Dirac-Fock program, *Comput. Phys. Commun.* **9**, 31-45 (1975)

S14. Furness J. B. & McCarthy I. E. Semiphenomenological optical model for electron scattering on atoms, *J. Phys. B: At. Mol. Phys.* 6, 2280 (1973)

S15. Koshino M., Tanaka T., Solin N., Suenaga, K., Isobe, H. & Nakamura, E. Imaging of Single Organic Molecules in Motion. *Science***, 316***,* 853-853 (2007)

S16. Somada H., Hirahara K., Akita S. & Nakayama, Y. A molecular linear motor consisting of carbon nanotubes. *Nano Lett.***, 9,** 62-65 (2009).

S17. Warner J. H., Ito Y., Rümmeli M. H., Büchner B., Shinohara H. & Briggs G. A. D. capturing the motion of molecular nanomaterials encapsulated within carbon nanotubes with ultrahigh temporal resolution. *ACS Nano.* **3,** 3037-3044 (2009).

S18. Erdemir D., Lee A. Y. & Myerson A. S. Nucleation of crystals from solution: classical and two-step models. *Acc. Chem. Res.* **42,** 621-629 (2009).

S19. Sosso G. C., et al. Crystal nucleation in liquids: open questions and future challenges in molecular dynamics simulations. *Chem. Rev.* **116,** 7078-7116, (2016).

S20. Loh N. D., et al. Matsudaira Paul & Mirsaidov Utkur, Multistep nucleation of nanocrystals in aqueous solution. *Nat. Chem.* **9**, 77-82, (2017).

S21. Qin L.-C. Determination of the chiral indices (n, m) of carbon nanotubes by electron Diffraction. *Phys. Chem. Chem. Phys.*, **9,** 31 (2007).

S22. Zoberbier T. et al. Interactions and reactions of transition metal clusters with the Interior of single-walled carbon nanotubes imaged at the atomic scale. *J. Am. Chem. Soc.* **134**, 3073 (2012).

S23. Spencer N. D., Schoonmaker R. C. & Somorjai G. A. Structure sensitivity in the iron single-crystal catalysed synthesis of ammonia, *Nature,* **294**, 643-644, (1981).

S24. Chen Y.-X. et al. Tuning the shape and catalytic activity of Fe nanocrystals from rhombic dodecahedra and tetragonal bipyramids to cubes by electrochemistry, *J. Am. Chem. Soc.* **131,** 10860-10862, (2009).

S25. Powell C. J., Jablonski A., Salvat F. & Lee A. Y. NIST Electron Elastic-Scattering Cross-Section Database, Version 4.0. https://www.nist.gov/publications/nist-electron-elastic-scattering-cross-section-database-version-40 (2016).